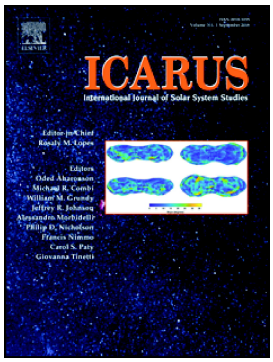

Chandrayaan-3 landing site evolution by South Pole-Aitken basin and other impact craters

S. Vijayan, K.B. Kimi, Anil Chavan, R. Aditi, U. Thahira, V. Rama Subramanian, Rishitosh K. Sinha, Amitabh, Santosh Vadawale, M. Shanmugam, N.P.S. Mithun, Arpit R. Patel, S. Amit Basu, K.V. Iyer, K. Suresh, Ajay Prashar, G. Rima, Anil Bhardwaj

PII: S0019-1035(24)00389-0

DOI: https://doi.org/10.1016/j.icarus.2024.116329

Reference: YICAR 116329

To appear in: *Icarus*

Received date: 25 February 2024

Revised date: 18 September 2024

Accepted date: 19 September 2024

Please cite this article as: S. Vijayan, K.B. Kimi, A. Chavan, et al., Chandrayaan-3 landing site evolution by South Pole-Aitken basin and other impact craters, *Icarus* (2024), https://doi.org/10.1016/j.icarus.2024.116329

Chandrayaan-3 landing site evolution by South Pole-Aitken basin and other impact craters

Vijayan S[1]., Kimi K.B[1]., Anil Chavan[1], Aditi R[2], Thahira U[3], Rama Subramanian V[1], Rishitosh K Sinha[1], Amitabh[4], Santosh Vadawale[1], Shanmugam M[1], Mithun N. P. S[1]., Arpit R Patel[1]., Amit Basu S[1]., Iyer, K. V[4]., Suresh, K[4]., Ajay Prashar[4]., Rima G[5]., Anil Bhardwaj[1]

[1]Physical Research Laboratory, Ahmedabad, India

[2]Institute of Remote Sensing, College of Engineering, Anna University, Chennai, India

[3]Department of Remote Sensing, Bharathidasan University, Trichy, India

[4] Space Applications Centre, Indian Space Research Organisation, Ahmedabad, India

[5] U.R. Rao Satellite Centre, Indian Space Research Organisation, Bangalore, India.

Corresponding author: vijayan@prl.res.in

Key points:

Chandrayaan-3 Pragyan rover images analysed for the first insitu crater distribution at Lunar high latitude south polar region

Chandrayaan-3 Vikram lander landed over ~2300 m of ejecta deposited from the South Pole Aitken basin and other basins/craters

Chandrayaan-3 mission landed within a buried impact crater, which is likely older than SPA basin

Abstract

The Chandrayaan-3 mission with the Vikram-lander and the Pragyan rover landed in the high latitude highland region near the south pole of the Moon. The landing site is located ~350 km from the South Pole-Aitken basin rim, an ancient and highly cratered terrain. This site has undergone the complex emplacement sequence of SPA basin ejecta followed by the nearby and distant impact basins and crater ejecta materials. To evaluate the source of individual basin and crater ejecta emplacement over this landing site, we carefully demarcated the nearby and distal basins and craters that could have contributed to the source regolith material. We found that the SPA basin is the major contributor, which deposited nearly ~1400 m of ejecta materials, and 11 other basins deposited ~580 m of ejecta. The other complex craters contributed up to ~90 m of ejecta. Meanwhile, secondary craters of a few km in diameter located adjacent to the landing site contributed to ~0.5 m ejecta, which are crucial target materials for the Pragyan rover insitu analysis. Pragyan rover images revealed the landing site is devoid of >1 m boulders along the traverse revealing typical highland terrain. The Pragyan rover Navcam and Optial High Resolution Camera regional images revealed linear distal ejecta rays possibly from the distant impacts as insitu evidence of foreign material at the CH-3 landing site. We found a semi-circular, heavily degraded structure encompassed around the landing site, which is interpreted as a buried impact crater ~160 km in diameter probably formed before the SPA basin. The erasure of pre-SPA basin craters is caused by both the direct burial by SPA basin ejecta, high seismic shaking during SPA formation, and then followed by various post-SPA craters and its associated some of the degradation processes. Overall, Chandrayaan-3 landed within an ancient region that hosts some of the most deeply excavated materials on the Moon.

1. Introduction

Impact crater density, distribution and degradation have been used as an indicators of the relative changes over the lunar surface (Head, 1975; Neukum et al., 1975; Robbins 2019, Wang et al., 2021). The crater density or superposed craters provides direct evidence for resurfacing or altering craters over the lunar surface (Basilevsky, 1976; Head et al., 2010; Kirchoff et al., 2013; Riedel et al., 2020). The crater degradation will be more extensive and significant if they are near to other bigger complex craters or impact basins due to ballistic sedimentation and secondary cratering (Oberbeck et al., 1973; Oberbeck, 1975; Fassett et al., 2012). The ejecta emplacement from the complex craters and impact basins will mantle pre-existing craters that are in the vicinity of the impact and this process significantly affects the older craters (Osinski et al., 2011; Xie and Zhu, 2016; Xu and Xie, 2020). Impact basin-forming events ultimately hinders and alters the pre-existing crater density adjacent to the basin and also mantles the older craters (Fassett et al., 2011). Such a process will reduce the pre-existing crater depths and alter the crater rim, central peak, and floor morphologies. This challenge leads to the impact record of the most ancient lunar terrains as being incomplete due to ejecta mantling by younger, larger impacts/basins. The survival of simple craters close by to basin rims is impossible; however, larger craters may survive the formation of basin continuous ejecta if they are even within two crater radii from the centre (Eggleton and Schaber, 1972). Such a process of erasing the older craters with new impacts will cause the population of visible craters to enter a steady state (Gault 1970; Woronow, 1978). This ejecta emplacement makes exploring ancient lunar terrains with high crater density like the lunar south pole region very challenging.

An impact basin near any landing site raises the question of how much millions of square kilometres are modified by the basin ejecta mantling, how much material could be excavated by these basins, whether deeper crustal or upper mantle material was excavated by basins, and how far the spreading occurred radially from the impacts (Head 1974; Howard et al., 1974;

Melosh 1989; Moriarty et al., 2021). One of the most well characterised basin ejecta emplacement process is by the Orientale ejecta, in which the ejecta thickness of ~2.8 km is deposited near the basin rim (Fassett et al., 2011). Apart from the ejecta, basin-forming impacts also produce secondary craters, which can approach primary crater size within the close vicinity of the basin rim (Fassett et al., 2011; Guo et al., 2018) or 5% of the basin diameter (Bierhaus et al. 2012; Schultz and Singer, 1980). Such an emplaced large crater will destroy pre-existing craters, which will, in turn erase the records of craters (Riedel et al. 2020). Thus, it is indeed essential to understand the lunar landing sites with their surrounding complex and impact basin's ejecta emplacement mechanism.

On August 23, 2023, 12:34 UT, the Chandrayaan-3 Vikram lander successfully soft-landed in a high-latitude region named Shiv Shakti Point (69.367621˚S, 32.348126˚E) (Fig. 1). Chandrayaan-3 Vikram lander landed ~350 km northeast from the rim of the South Pole-Aitken (SPA) basin in Nectarian age terrane (Sinha et al., 2019; Sinha et al., 2023; Fortezzo et al., 2020). On the same day, the Pragyan rover deployed from the Vikram lander and traversed for one lunar day. The Pragyan rover carries two Navigational Cameras (Navcam), one rear camera, an Alpha Particle X-ray Spectrometer (APXS) (Shanmugam et al., 2020; Mithun et al., 2020) and an Laser Induced Breakdown Spectroscopy (LIBS) (Laxmiprasad et al., 2013). The APXS instrument enables the qualitative and quantitative elemental analysis and derive the chemical composition, whereas the LIBS instrument can determine the elemental composition of regolith around the rover traverse region.

The main objective of this mission was to demonstrate the ability to achieve a soft landing in a high-latitude region, engage in roving activities in the vicinity, and conduct a series of in situ experiments, which was successfully completed. The mission lasted for ten days till September 2, 2023. The landing site is surrounded by several degraded complex craters ─ Manzinus

(diameter (D) ~96 km) to the north, Boguslawsky (D ~95 km) to the south, Boussingault (D ~128 km) and Boussingault A (D ~75 km) to the southeast, and Boussingault E (D ~104) to the east (Fig. 1). The Chandrayaan 3 landing site contains light plains deposits (Meyer et al. 2020), which have been interpreted as the impact ejecta (Wilhelms, 1965, 1970; Eggleton and Schaber, 1972; Muehlberger et al., 1972; Oberbeck, 1973) and/or volcanic materials (Trask and McCauley, 1972). A detailed study of the Boguslawsky region, which was a tentative landing site of the Luna-Glob mission, is near the Chandrayaan 3 landing site, revealed that the light plains in Boguslawsky were likely caused by local impact ejecta, ruling out the volcanic hypothesis as there were no discernible volcanic sources or features present (Ivanov et al., 2017). The ejecta distribution around the Chandrayaan-3 landing site is important to understand the origin of material, the depth of excavated material distributed over this site, and the nature of modification that occurred over the geological timescale. The goal of this study was to understand the role and influence of basin-forming impact and complex craters influence in and around the Chandrayaan-3 landing site. This study also evaluates the results of small-size crater density derived from the Navigation Camera on the Pragyan rover (Navcam) along its traversed path, comparing these findings with data from the Orbiter High-Resolution Camera (OHRC) on board the Chandrayaan 2 orbiter. We expect that the crater morphological comparison with high latitude in-situ exploration will provide clues to their degradation and state of retention. This paper presents a workflow to coordinate and analyse the orbiter and rover derived images for the crater distribution around the Chandrayaan-3 landing site.

2. Data and Methods

In this study, we used the Chandrayaan 2-Orbiter High-Resolution Camera (OHRC) of spatial resolution ~0.25 m (Chowdhury et al., 2019), which allowed us to capture a comprehensive view of the features present in the study area. For topographic measurements, we used the

merged data of the Lunar Orbiter Laser Altimeter (LOLA) and Selenological and Engineering Explorer (SELENE)-Terrain Camera (TC) digital elevation model (DEM) with a spatial resolution of ~59 m/pixel and a vertical resolution ~3–4 m (SLDEM 2015) (Barker et al. 2016). Subsequently, for on-site investigations, we analysed images acquired by the Chandrayaan-3 Pragyan rover Navcam images (Subhalakshmi et al., 2010; Laha et al., 2018).

We conducted crater mapping in the landing region within the buffer of 100-meter diameter using the Chandrayaan 2-OHRC using orthographic projection. Along with the craters, we also identified striations associated with the impact ejecta. Subsequently, we extended our crater mapping efforts by utilizing images captured by the Navcam along its traversed path, followed by a comparative analysis. Based on the mapping from OHRC images, we selected the craters that contributed ejecta to the landing site. Further, we extended to complex craters around the South Polar region at least 300 km surrounding the Chandrayaan-3 landing site. We analysed each crater, which can deposit their ejecta at the landing site. The list of chosen craters, their diameter, and their distance from the landing site is given in Supplementary Table 1. In our work, we used the ejecta thickness estimation formula based on the diameter of the craters. For smaller craters with a diameter range from 3 to 45 km we used the Sharpton (2014) model for the ejecta estimation. For craters>45 km, we used the Housen et al. (1983) model for the ejecta estimation. For impact basins >300 km we used the Fassett et al. (2011) formula for the ejecta estimation. We also computed the ejecta thickness from Pike (1979) within 100 m region surrounding the landing site.

1. (McGetchin et al., 1973) model

$$thickness = 0.14R_t^{0.74}(r/R_t)^{-3}$$

2. (Pike 1974) model

$$thickness = 0.033R_t(r/R_t)^{-3}$$

3. (Housen et al., 1983) model

$$thickness = 0.0078R(r/R_t)^{-2.61}$$

4. (Fassett et al. 2011) model

$$thickness = 2900(r/R_t)^{-2.8}$$

5. (Sharpton 2014) model

$$thickness = 3.95R_t^{0.399}(r/R_t)^{-3}$$

Where r is the radial distance from the crater centre in meters, R_t is the rim radius of the crater/basin. The evolution of these models is extensively studied by earlier works, and these models provide a first-order estimates about the ejecta thickness over the CH-3 landing site. The landing site is covered by secondaries, simplex, complex craters and impact basins. So, we adopted a different model based on their empirical nature we assigned to each size of the craters (Krasilnikov et al., 2022). Supplementary Table 1 provides the ejecta estimation from all the models.

3. Results

3.1 Crater distribution around the Chandrayaan-3 landing site

Between -60 S to -90 S, there are at least 120751 craters with diameters >1 km(Robbins, 2019). For crater distribution around the CH3 landing site within a 50 m radius of the lander we counted the craters from CH-2 OHRC images. Though the path of the Pragyan rover is mainly towards the west of the Vikram lander, we mapped the craters around the Vikram lander (Fig. 3a). From the CH-2 OHRC images, we mapped the craters within 50 m radius from the

Ch-3 landing site. We mapped 671 craters, the smallest and largest crater diameter are ~0.65 m, and ~16 m, respectively. This distribution indicates that the CH-3 lander landed within a zone where a large number of small craters are distributed, which includes both the primary and secondary craters. Mahanti et al., (2018) mapped the craters >35 m over the Apollo 16 landing site and revealed that nearly 70% of the craters are degraded.

To correlate the Chandrayaan-2 OHRC orbiter-identified craters with the insitu rover identified, we carefully scouted and identified each crater from the Navcam images (Fig. S1-S16). The Pragyan rover Navcam images are suitable within the first 5 m range. Further away, upto 30 m, the images are ideal for only counting the craters and for such distant craters we did not estimated the diameter. To delineate the craters from Navcam and orbiter, we carried out a 5m buffer region upto 30 m along the rover traverse, which provides the maximum distinguishable feature from each Navcam image. The same 30 m buffer distance from the Navcam images is also created in the OHRC images (Fig. 3b). Then, we visually compared both the images and carefully delineated the craters visible in both Navcam and OHRC. Fig. S1-16 shows the rover Navcam images at each stop and the visible extent of each craters can be distinguished. Some of the craters around the Chandrayaan-3 landing site from the rover Navcam are shown in Fig. 4. Interestingly, we observed that within a 10 m crater (Fig. 4a), there are at least ten even smaller craters, which reveals the impact flux in a small region. This 10 m crater (Fig. 4a) lacks boulders over its rim. From Fig. 4, it is also evident that the crater walls are smooth and not sharp. We carefully counted the craters from each image, taking care of several overlaps within the acquired Navcam images. We were able to distinguish and map nearly 111 craters from the rover Navcam to the orbiter image (Fig. 3b). However, we observed there are plenty more craters that are only observed in the rover Navcam and not distinguishable from the orbiter. Thus, the total number of craters that are counted from the rover Navcam images are 179 craters. Within the 50 m radial path, the number of craters from the orbiter to

in-situ images revealed that the crater density is nearly 50% more. This flux of impact craters we observed from the rover images are mostly superposed craters, small diameter and they mostly appear in clusters and this tend to be secondaries (Fig. 3a).

3.2 Ejecta thickness around the Chandrayaan-3 site

Fig. 2a shows the CH2-OHRC image with the Vikram lander and the Pragyan rover traverse and Fig. 2b shows the topographical variations over the landing site. The Vikram and the Pragyan landed and moved over the highland terrain comprised of regolith and ejecta emplaced from different craters. For the ejecta thickness estimation, we incorporated simple and complex craters in the vicinity of the landing site and their contribution of ejecta to the landing site. The ejecta deposited by the crater/basin was classified into different thickness levels <1 m, 1- 10 m, and >10 m (Fig. 5), which makes it possible to identify the sources of the material and its share in the landing site. The ejecta deposits vary significantly based on the crater diameter. Within the stereographic projection south pole image (Fig. 5), the complex craters have distributed tens of meters of ejecta over the landing site. The oldest and probably the first ejecta material to get deposited at the landing site is the South Pole-Aitken basin ejecta material (SPA). The SPA basin rim (Kring and Durda, 2012) is ~350 km away from this landing site. The estimated ejecta deposits from the SPA basin using the Fassett et al., (2011) model is ~1400 m. Other impact basins from the mid-latitudes and even from the near-equatorial region distributed the ejecta material, and they count for 10 to 100 m of thickness (Fig. 5). The complex craters near the landing site contributed to 10's of meter of ejecta, whereas the complex craters ejecta thickness varies over their corresponding distance (Fig. 5). We observed two large individual secondary crater clusters ~2 and ~3 km in diameter (Fig. 5), and this is the most probable closest large secondary crater to the landing site. Considering the ejecta from multiple craters deposited over the landing site, we constructed a stratigraphy of ejecta deposits. The stratigraphy of ejecta deposits over the Chandrayaan-3 landing site is shown in Fig. 6. The

largest contribution is from SPA (~1400 m), followed by ejecta by 12 impact basins (~580 m), complex craters (~90 m), and finally, the simple and secondary craters

4. Discussion

4.1 Ejecta rays at Chandrayaan-3 site

Lander and rover missions to the Moon are mainly surveying or analysing the top most regolith (Langevin and Arnold, 1977; Mckay et al., 1991), although some observed the drill core depth relationships (Carrier III, 1974). The topmost regolith layer is the most crucial region because the material could be in situ-originated or emplaced from a distance by impact craters. Without knowing the source for the topmost regolith layer, the analysis and the interpretation will vary accordingly. The high crater density in the highland region surrounding the lander suggest that the landing site region regolith is most likely dominated by distal materials emplaced by the impacts (Fig. 5). In addition, the highland craters around the rover traverse (Fig. 3c) are shallower, which is consistent with shallow crater depths (Wu et al., 2022) and weathered insitu over the geological timescale (Povilaitis et al., 2018). This brings the need for the contextual analysis of the landing site with the surrounding nearby and distant craters, which has the potential to overturn regolith (Speyerer et al. 2016) or mantling by thick/veneer distal ejecta ray materials (Xiao et al., 2021; Xie and Xu 2020). A cluster of secondary craters along with well-defined rays from the Tycho crater is observed at the Apollo 17 landing site (Arvidson et al., 1976; Lucchitta, 1977). This is one of the preliminary works that proposed the possibility of crater transporting material to distal locations. The distance between these two locations is more than 2000 km. The orbiter-based analysis from the Clementine and Lunar Prospector missions also suggests that the Tycho component at Apollo 17 was likely anorthosite troctolite to anorthositic norite (Fruland et al., 1977; Petro and Pieters, 2006). Though the geological

arguments are there for the presence of Tycho rays on the Apollo 17 site, the larger the craters, the further distal region the ejecta can reach is evident (Hawke et al., 2004).

Fresh craters are known to produce bright ejecta rays distinct from primary ejecta, which is spread to several crater radii (Hawke et al., 2004; Elliott et al., 2018). Such ray material will gradually decay from the impact and at the farthest point 5 crater radii from rim it contains distal ejecta materials (Osinski et al.,2022), which mantle the top most lunar surface. For example, Fig. 7a shows the Tycho crater and the ejecta ray extending to at least 15 crater radii (Dundas and McEwen, 2007). Fig. 7b-d shows example of such distal ejecta rays with linear groove like features at different locations around the Tycho crater. The young age of the Tycho (Arvindson et al., 1976; Hiesinger et al., 2012) lead to the preservation of such distal ejecta rays with distinguishable parallel linear features.

We have taken forward these interpretations and observed such linear and radial distal ejecta ray features around the CH-3 landing site and found several linear groove-like features to the SE of the CH-3 landing site (Fig. 7e). The Chandrayaan-2 OHRC image (Fig. 7e) clearly distinguishes the linear feature adjacent to the landing site, and this could be a distal ejecta ray from the distant crater. From Fig. 5, it is evident that there are several fresh craters that could have emplaced ejecta and that are radially oriented to the SW of the landing site, in particular Schomberger and Schomberger A. To identify whether the Schomberger and Schomberger A are the potential craters, which formed these distal ejecta rays around the landing site, we examined our ejecta thickness estimation map (Fig. 5). From that, we interpret that these two craters are radially aligned to the landing site, located towards the SW direction of the landing site, and relatively younger complex crater over this region and host distinguishable radially ejecta and secondaries (Fig. 5). Our estimation of ejecta thickness (Fig. 5) from these two craters suggest that ~4 m and <1 m by Schomberger and Schomberger A, respectively. Also

from Fig. 5 it is evident that proximity linear grooves and distant secondaries are oriented radially from these two craters. This brings the consensus of opinion that these craters are likely candidate for the linear groove-like features observed around the Chandrayaan-3 landing site (Fig. 7c). If this is the case, then Schomberger and Schomberger A, are situated almost on the rim of the SPA basin, where the deeper crustal materials are located (Vadawale et al., 2024).

However, the two large secondary crater clusters near the landing site also contributed to ~0.5 m of ejecta over the landing site (Fig. 3). Though the secondary crater-driven ejecta distribution is small, there are recent impacts, and their ejecta emplacement over the landing site will be the potential target for Pragyan rover in-situ analysis instruments like Alpha Particle X-ray Spectrometer (APXS) (Mithun et al., 2020) and Laser Induced Breakdown Spectroscopy (LIBS) instruments (Laxmiprasad et al., 2013). The secondaries craters near the landing site region will churn, redistribute and bring the subsurface material to the surface, which is likely analysed by the instruments on board the Pragyan rover. Because these instruments will observe the top few micrometres of the surface, the source for the target needs to be understood to interpret the in-situ chemical composition analysis. However, the complex craters around the landing site are mixing and redistributing the SPA ejecta material. This continuous redistribution of the SPA ejecta is likely to make the Chandrayaan-3 region be homogeneous distribution of SPA ejecta.

Interestingly, a similar kind of linear, parallel ray-like structure was observed close to the landing site from the rover Navcam image (Fig. 8). Within 10 m away from the lander, we observed this linear feature, and two possible scenarios are possible. This could be the blast from the lander while landing on the lunar surface as suggested in previous studies (Roberts, 1963; Clegg et al., 2014). However, no such rays are observed near to Vikram lander (Fig. S6, S7), though the Vikram lander hovered before the landing at ~150 m height. If this linear ray-

like feature is an output of the lander, then it should be evident from the images adjacent to the lander (Fig. S6). We envisage that this could be the distal ejecta ray-like material emplacement over the landing site. We have also observed similar linear ray-like features from the Navcam image over two other locations. One is further south from the lander and one near the lander (Fig. S1, S4). If these are ejecta rays, these are the in situ evidence for the mantling of distant material over the landing site. This observation made us interpret that this could be possible distal material emplaced by impact craters.. Overall, Fig. 7e provides evidence for the emplacement of typical ray material adjacent to the landing site.

4.2 Chandrayaan-3 landing site Regolith

Regolith represents the build-up of a series of layers of impact ejecta materials from individual impacts over a period of time followed by space weathering (McKay et al., 1979). Smaller impacts or secondaries, which are more frequent and recent, tend to mix or garden the already present regolith which leads to lose many of the distinguishing characteristics of the original deposit (McKay et al., 1991). Similarly, the Apollo16 landing site received ejecta from the Mare Imbrium basin and nearby complex craters (Wilhelms et al., 1987, Petro and Pieters, 2006). The CH-3 region regolith deposits has been gardened by the subsequent smaller impact, which resulted in a finer regolith layer, and the thickness would be similar to ~6-10 m on the surface top (Freeman, 1981). Though the complex craters near CH-3 site excavated subsurface material, most likely they have redistributed the SPA ejecta that was emplaced over those regions (Fig. 5). However, SPA basin ejecta materials are mixed, redistributed by younger crater and re-exposed beneath material to form mixed regolith (Huang et al., 2018; Moriarty et al., 2020) and also includes impact melt rocks that may have differentiated (Melosh et al., 2017; Moriarty and Pieters, 2018). Xie et al., (2020) estimated the basin derived ejecta over the A16

site and the overall thickness tends to ~367 m, and the closest Nectaris basin contributed the most. Whereas in the case of the CH-3 site, the SPA basin ejecta thickness itself tends to ~1.4 km. However, the SPA basin would have led to thermal perturbations (Watters et al., 2009), a large volume of impact melt, that likely differentiated, in addition to other impactites (Hurwitz and Kring, 2014; Melosh et al.,2017; Uemoto et al., 2017; Moriarty and Pieters, 2018). Even though other impacts and distant basins contributed (Fig. 5), the dominant ejecta from SPA is mostly mixed by the younger impacts in the vicinity of the CH-3 site. Being a high latitude highland terrain, the role of intrusion magmatism is ruled out due to visually and spectrally indistinct from other terrain (Eliason et al.,1999; Ivanov et al., 2018), absence of both morphological features like lava fronts, and edifices, meaning the dominant resurfacing is due to the emplacement of crater ejecta (Meyer et al., 2019). Further to this emplacement, the ejecta material has undergone continuous space weathering and mixing by simple and secondary impact, leading to the formation of a regolith layer. Secondary craters are one of the prime sources for mixing the top regolith layer. Speyerer et al., (2016) study using the LRO-NAC images revealed that the secondary's shallow excavation would churn or garden the upper few centimetres of regolith. Also, in 8.1×10^4 yr., the top 2 cm of regolith will be mixed by reworking and gardening (Speyerer et al., 2016). A similar interpretation is provided by the Apollo drive core samples, which reported the top 10-50 cm of the regolith layer is locally reworked and homogenized (McKay et al., 1991). The Pragyan rover Navcam images also reveals the Ch-3 landing site regolith layer is fine-grained and lacks large pristine boulders. Most of the boulders are semi-buried (Fig. S1-S12) on the surface, evidence of several million-year timescale weathering. The Pragyan NavCam revealed the insitu crater density from the south polar region is the first evidence, which indicates the flux of smaller craters is relatively higher. Overall, the Chandrayaan-3 landing site host SPA basin ejecta along with other impact crater ejecta that

could be mixed or reworked or redistributed by the simple and secondary craters, leading to the redistribution of SPA basin ejecta within the landing site.

4.3 Crater degradation around the Chandrayaan-3 landing site

The Pragyan rover Navcam images provided insitu images of the south polar region of the Moon (Fig. S1-S16). The CH3 landed over a Nectarian terrain, where all the craters in the host surface are anticipated to be weathered due to the older geological epoch. Some of the craters encountered by the Pragyan rover are visually identified and compared to the OHRC image, whose resolution is 0.25 m/p (Fig. 9). Overall in the landing site and within the rover traverse there are two notable craters with a diameter of ~10 m located in the south and west direction of the lander (Fig. 9a). A part of the lander leg landed within a crater (Fig. 9b), where the crater is shallower and appears to be older. The old nature of this crater has minimal effect on the landing inclination. Such craters are widespread over this region (Fig.4 b, c). In front of the lander ramp, through which the Pragyan rover rolled down to the lunar surface, there is a crater with a diameter of <1 m. This is the first obstacle crater encountered by the Pragyan rover. This shallow crater lacks boulders, and the Pragyan rover's right side three wheels passed over this crater. The rover tracks are visible within this crater (Fig. 9b). This crater is almost the size of the rover itself, but with minimal depth the rover could pass through easily. There is no boulder at all around this crater, which indicates the weathering it has undergone post its formation. When the rover encountered a ~10 m crater in the south direction of the Vikram lander, it had to reverse back due to the large crater size, which hindered the forward movement of the rover path. This lack of boulders could be due to impact on regolith rich layer or the boulders weathered during the course of time, which is difficult to interpret. The landing site is a Pre-Nectarian terrain, and in agreement to that the craters are relatively old and lack boulders or mass wasting (Xiao et al., 2013).

The space weathering effects and its older formation age lead to this current status of low boulder rate (Ivanov et al., 2018; Watkins et al., 2019; Kawashima et al., 2022). Also, the regolith mantling over this crater wall is well evident from Fig. 9c. When the Pragyan rover was ~30 m spatial distance from the lander, it encountered a few craters with notable fractured boulders (Fig. 9 d, e). These craters have relatively higher depths than the other craters over this region. The shadow and the sunlight region are different for these craters, which is a visual indication to identify the depth. These craters are also adjacent to a relatively fresh crater on the west whose ejecta boulder could be distributed over this region. During the entire Pragyan traverse of ~103 m, there are a notable number of older craters, all of them degraded with shallow depths and lack of big boulders. The Yutu-2 rover, during its traverse, observed several craters surrounded by several large boulders (Dine et al., 2022) on the mare region. The older formation of these craters is one probable reason for their shallow depths and lack of boulders over the landing site region.

4.4 Crater deformation over the South Pole region

The ejecta thickness models reveal that the Ch-3 Vikram lander and Pragyan rover landed over a region where ~2300 m of ejecta deposits from different craters are deposited (Fig. 6). This large ejecta thickness over the landing site brings us an intriguing question: that what is the pre-existing topography of the region, how the vast volume of ejecta from different basins/craters were deposited and how they degraded the craters over the south polar region of the Moon. The LRO-WAC-derived topography image of the south pole region (Fig. 10) reveals many degraded/buried impact craters. The SPA basin rim is demarcated, and we searched for heavily degraded craters within and outside the SPA basin rim. There is a possibility of degradation within and outside the SPA basin rim. In the case of degradation outside the SPA

basin rim, they could be possibly due to the SPA basin ejecta emplacement or degradation by SPA secondaries or degradation by other large diameter complex craters post SPA. In the case of degraded craters within the SPA basin rim, it is only due to superposed complex, large diameter craters. We examined for any possibly preserved pre-SPA basin impact craters, which could host the SPA basin ejecta deposits. We come across several degraded craters without any circular rim, partially preserved rim, and heavily superposed craters, and some of the example craters are shown in Fig. 10, which are already identified as impact craters by Robins (2019). These craters are not circular because they are superposed by many complex craters, which leads to obliteration of their rims, floor, etc. In Fig. 10 b-h, the various diameter craters are shown which have degraded and lost their rim significantly. All these craters are identified as impact craters and catalogued by (Robbins, 2019). There is no possibility of survival of any crater close to the SPA rim because all of them would be obliterated or buried by the thick SPA ejecta. The craters that are away from the SPA basin rim and large in diameter, like Fig. 10 b, d, have a possibility that these can be before or post to SPA basin. In Fig. 10a, there are several craters within the SPA basin rim; those are larger diameter craters whose diameters are >100 km. Such craters are also highly deformed, but this deformation is due to heavy bombardment post to SPA formation or later. In general, it is evident from Fig.10 that the large diameter craters are highly degraded over the south polar region.

We have chosen several degraded craters within the SPA basin, a few adjoining the SPA rim and a few craters outside the SPA rim (Fig. S17a-c). The rims are discontinuous, eroded, and lack a circular shape. Such craters are direct indicators of degradation post-to-SPA basin formation. Fig. S17d-f shows the craters that are located adjacent to the SPA basin rim, and these craters also severally lost their rims, overlaid by multiple superposed craters, and are non-circular in shape. Some of the craters observed are adjacent to the SPA rim, and they likely formed post to SPA basin formation interpreted based on their highly degraded state and

superposed over the SPA rim. These craters are heavily degraded, and their odd-shaped structure with variable depth indicates their deformation. The Fig. S17g, h shows the degraded craters that are a few 100's km from the SPA rim. These craters are deformed, and interestingly, they are having shallow depths when compared to other craters in this region. This decrease in depth suggests they are old and degraded, but the clarity is not satisfactory as to whether these could be pre-SPA basin impacts. The diameter of these craters is not that big, so the probability of the chance of their pre-SPA basin formation is not likely. Such highly obliterated, degraded craters, topographic variations are already present in the south pole region of the Moon (Krasilnikov et al., 2023). This suggests that the south polar region craters, which are post-formation to the SPA basin, are highly modified and reveal the high rate of crater degradation by superposed craters.

4.5 Evolution of Chandrayaan-3 landing site

The south pole region is one potential destination of several future human and lander-oriented missions. To understand the pre-existing topography of the Ch-3 landing site region, we extended our analysis into a regional perspective and observed a near semi-circular structure present over the CH-3 landing region (Fig. 11). This semi-circular structure with a best-fit circle forms a diameter of ~160 km that we anticipated to be a degraded impact crater. However, we are sceptical about the semi-circular structure and examined it further. On reviewing Fig. 11, we observed several of the south polar highland craters are not circular nor retained their rims (Fig. 10). These are due to the degradation by the younger impacts and the topography. A similar condition can be applied to the CH-3 site observed degraded crater. We compared these likely buried craters to the other established degraded craters (Robbins 2019)

and interpreted that the SPA formation, their ejecta emplacement, and the other complex craters over this region have potential effects in degrading the crater signature.

To verify this buried crater interpretation, we compared similar diameter craters over the south polar region including Ashbrook (~157 km), the unnamed crater at 80 S 192 E and west of Schrodinger basin (~161 km), Drygalski (~162 km), Hausen (163 km) (Fig. 11). Based on the crater depth to diameter ratio by Pike (1974), the first-order average depth of ~160 km crater is ~4.8 km. To validate our interpretation of this buried crater, we plotted the topographic profile of all the above four craters, which is shown in Fig. S18. The relatively fresh craters like Drygalski and Hausen have a depth of ~5 km, which reveals that over the south pole highland region an impact crater of ~160 km diameter will have a depth of ~5 km. Interestingly, two craters Ashbrook and unnamed crater are mantled by the nearby impact crater/basin ejecta Drygalski and Schrodinger which significantly reduced the crater depth due to the emplacement of ejecta. In addition, we measured the current depth of this buired crater, which is ~2 km. Our ejecta estimation over this CH-3 site revealed a thickness of ~2.4 km. Summation of this tend to ~4.4 km, which is nearly equivalent to a ~160 km diameter crater depth. However, a small difference in depth could be due to the slumping of material within the buried crater, impact velocity, angle, etc., which further reduces the depth. This can be explained in the following way; the buried crater depth is further decreased by the deposition of SPA basin ejecta over the other parts of the crater walls and which slides down and deposits over the floor. This will significantly have decreased the depth of the crater, thereby adding more SPA basin ejecta material over the floor. This is a well-known phenomenon in complex craters which are near large impact basins. For example, the two large craters located to the East of the Orientale basin, Lamarck D (~131 km diameter) and Darwin (~122 km diameter), host slumped Orientale ejecta materials along their walls (Fassett et al., 2011). This makes their floor very hummocky, and they are approximately 100 and 200 km, respectively, far away from the eastern rim of the

Orientale basin. Although several pre-Orientale craters (like Blackett, Gerasimovich, Houzeau, Elvey) are hosting the Orientale ejecta material, these craters provide a similar scenario and likely support the possibility for the Chandrayaan-3 landing site crater buried by SPA basin ejecta materials.

5. Conclusion

Impact crater studies using orbiter and in-situ Pragyan rover Navcam images lead to the identification of several new small craters by the rover Navcam. The comparison of insitu rover images with the high-resolution orbiter images revealed that a significant number of smaller craters are only visible from the insitu imaging. This indicates the crater density and flux are much higher than those estimated from the orbiter. Though the craters encountered by the rover are smaller in size, significantly a large number of craters with eroded nature reveal space weathering and degradation on impact craters. The coordinated observation from rover and orbiter images suggests that the boulder population densities are significantly less around the Pragyan rover traverse and the craters over the Chandrayaan-3 landing site are severely degraded. This crater degradation and the boulder breakdown and degradation rate is one of the significant contributions to the lunar highland regolith. Our interpretation from the regional exploration over the Chandrayaan-3 landing site revealed a near semi-circular like structure, which likely indicates a degraded crater by the SPA basin ejecta. From our geomorphological analysis that the Chandrayaan-3 landing site was located within a buried impact crater of ~160 km diameter. However, further analysis by comparing the other south pole highland craters revealed most of the Nectarian craters have undergone severe degradation, whose rims are nearly 50% obliterated or buried or degraded by other impacts. This inter-comparison approach provided confidence in the degradation of such Nectarian to Pre-Nectarian craters by impact

basins. Overall, our study reveals that the Chandrayaan-3 Vikram lander and Pragyan rover landed within a possible buried crater, which is hosting the SPA basin ejecta material.

Acknowledgement

All the authors thank Department of Space, Indian Space Research Organisation for the Chandrayaan-3 mission. We thank Dr. Gordon Osinski and Dr. Patrick C. Pinet for their insightful suggestions. We thank the ISRO team for making the instruments for the Chandrayaan-2 & Chandrayaan-3 missions. We thank the makers of LRO-NAC/WAC, Kaguya, and https://quickmap.lroc.asu.edu/.

Figures

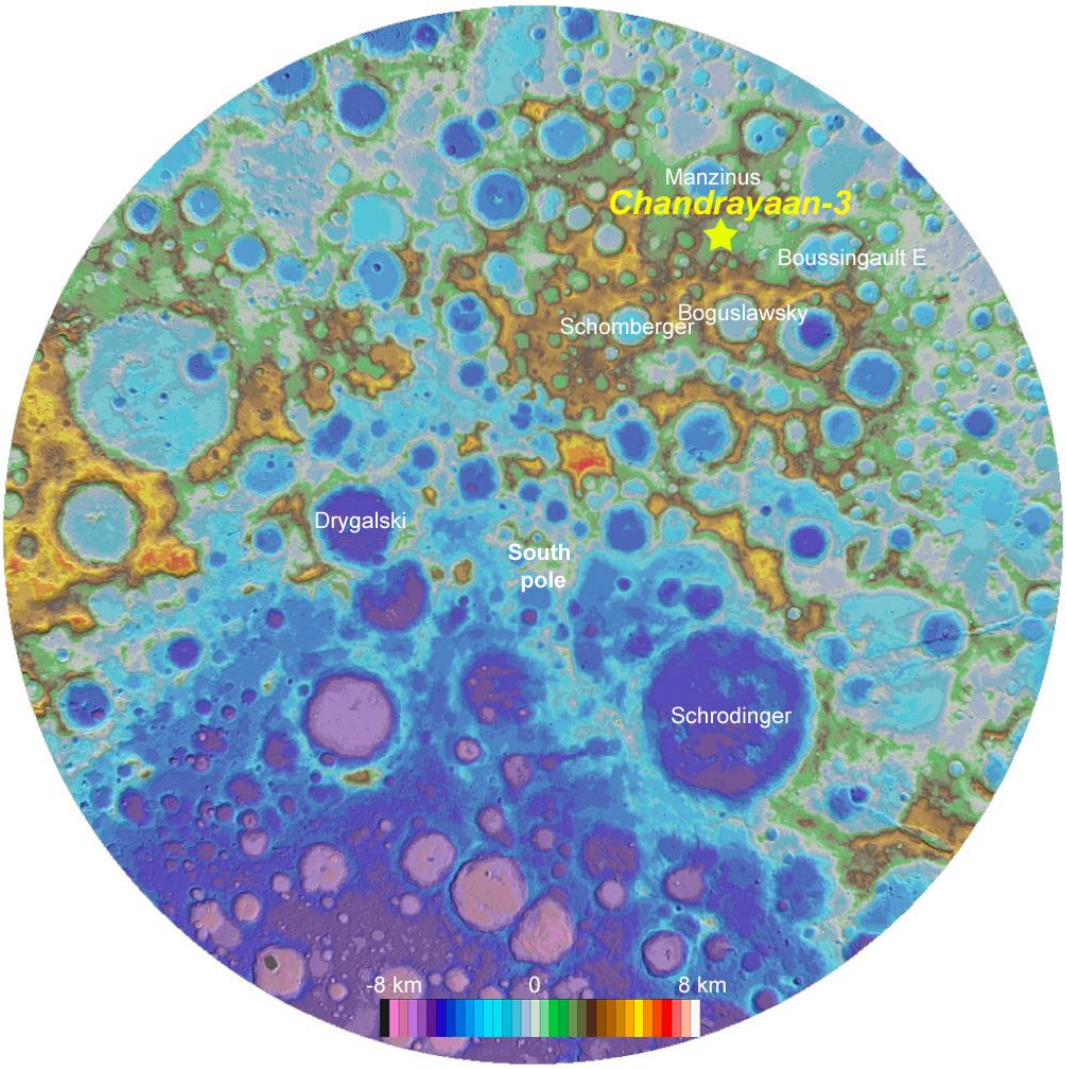

Fig. 1 LRO-WAC stereographic South pole DTM image with the location of Chandrayaan-3 landing site. Note the Ch-3 site is located in one of the elevated regions over the south pole region. The large number of craters over this region is a typical representation of the highland region and several degraded craters are also present over the site.

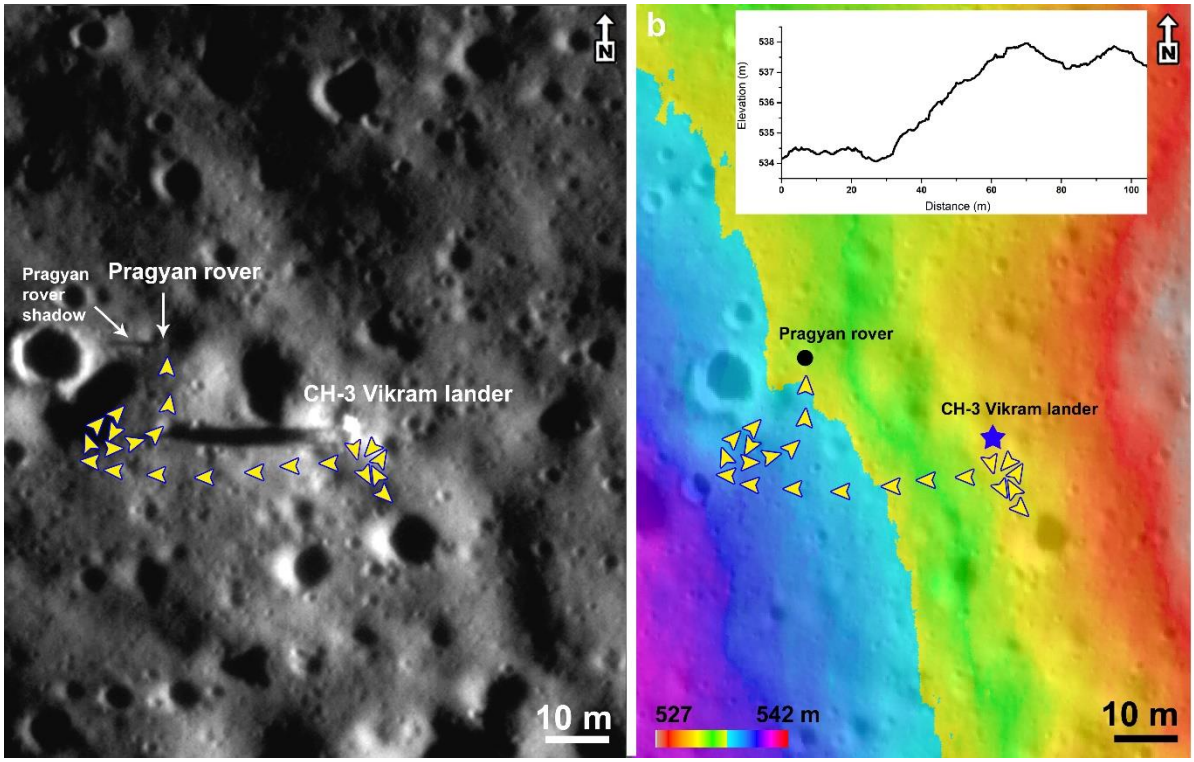

Fig. 2 a) Chandrayaan-2 OHRC image (ch2_ohr_ncp_20240315T2053268535_d_img_d18) with Chandrayaan-3 Vikram lander and Pragyan rover on the lunar surface. The Sun is located in the east side of the image, which illuminated the lander/rover and casted a long shadow. The yellow arrow indicates the path traversed by the Pragyan rover, b) The Chandrayaan-2 OHRC derived DEM shows the topographic variation around the landing site. The inset image shows the Pragyan rover traverse path elevation variation. When the rover moves westward there is an increase in elevation.

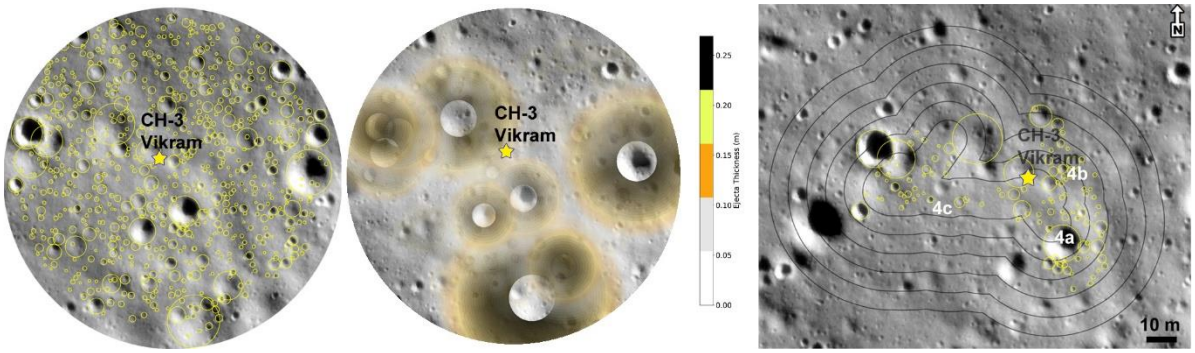

Fig. 3 a) Crater distribution within 100 m from the CH-3 landing site mapped using the Chandrayaan-2 OHRC image (ch2_ohr_ncp_20200826T0303458884_d_img_d18). No fresh craters with distinguishable ejecta are present over the landing site, b) Within the 50 m radius around the Vikram lander the contribution of ejecta from multiple smaller craters are computed using the Pike (1974). These small crater redistributed the ejecta material within the landing and such materials are targeted by the instruments on board the Pragyan rover, c) The Pragyan rover traverse path buffered at 5m interval upto 30 m to map the craters that are visible from the rover Navcam images. The craters marked within this 30 m buffer region are visible and identified from the OHRC image.

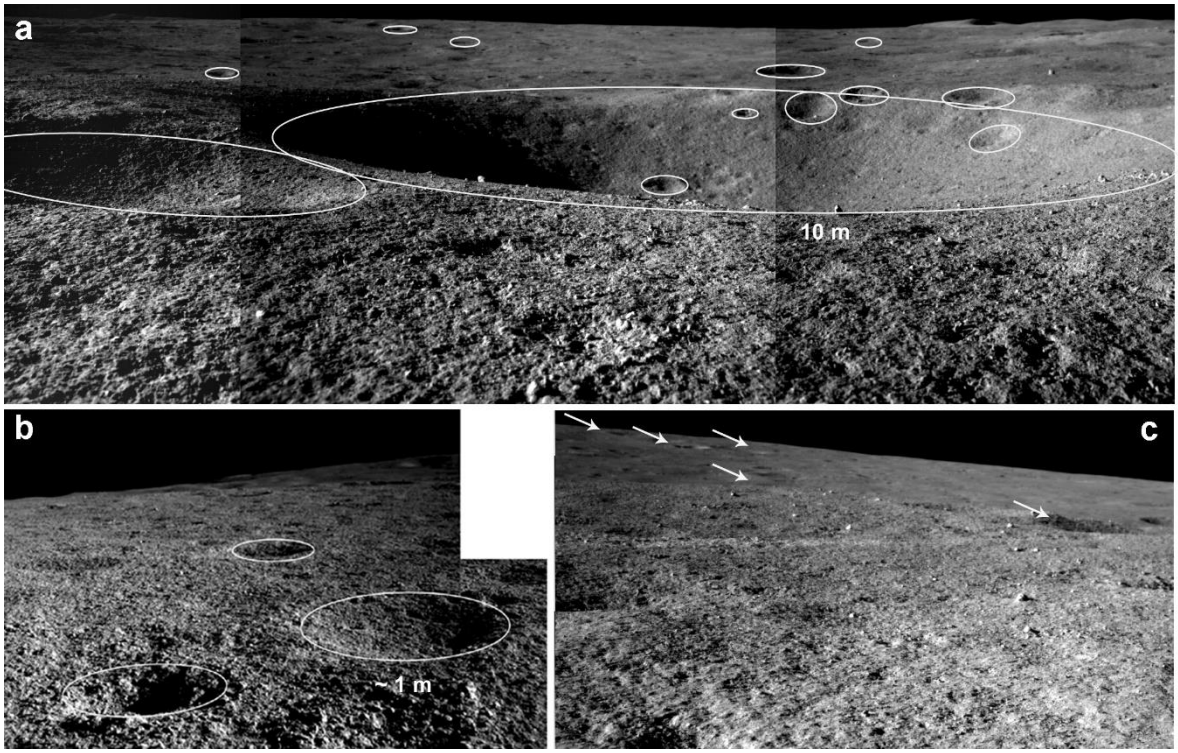

Fig. 4 The Pragyan rover Navcam images a) mosaic of several images to show the ~10 m crater located south of Vikram lander, b) Navcam image from west of lander with craters hosting few distinguishable boulders, but smaller in size, c) Navcam image from east of lander with craters visible over the horizon. For locations of craters refer to Fig. 4c.

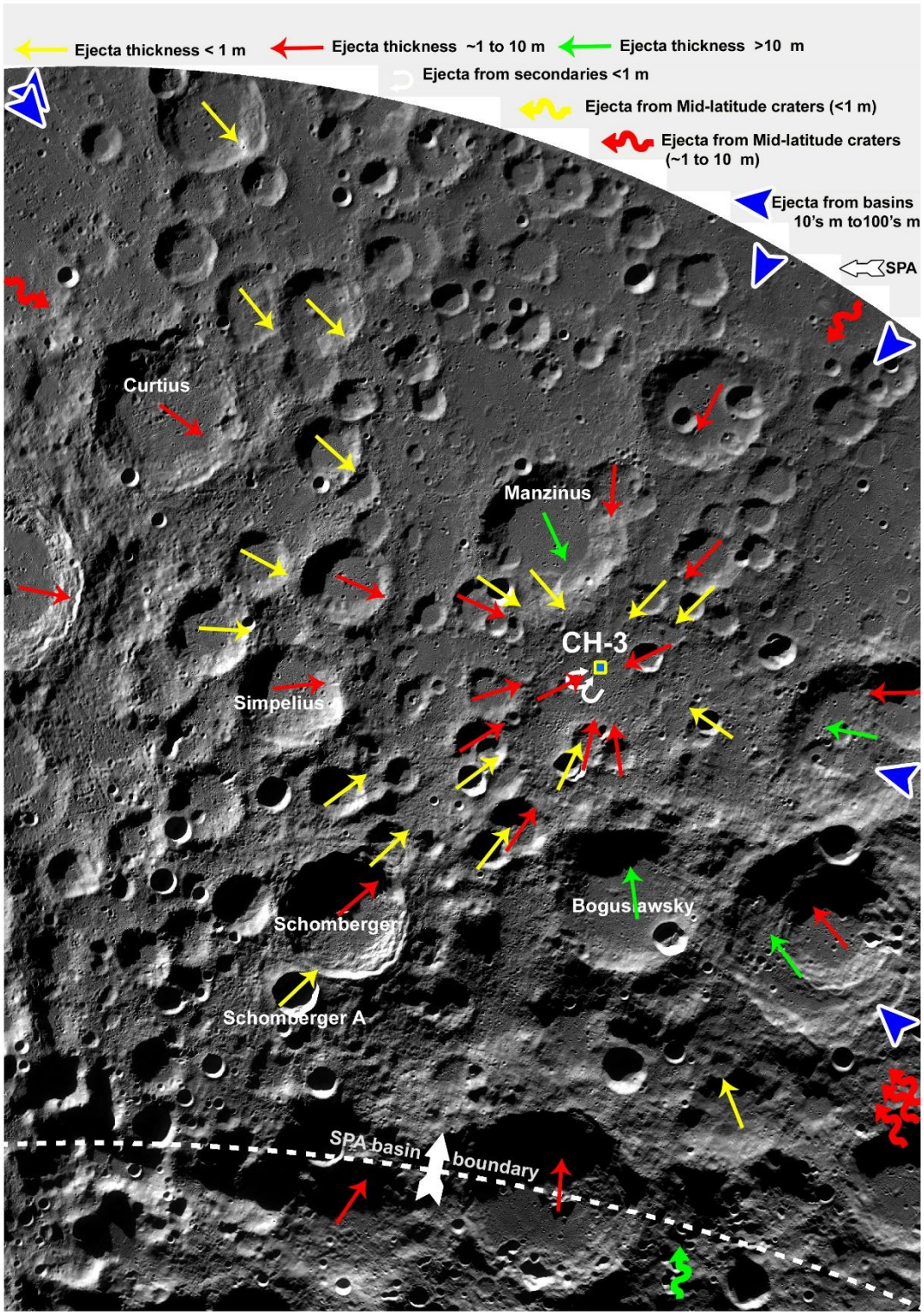

Fig. 5 The LRO-WAC stereographic South pole image with the Chandrayaan-3 landing site and the arrows indicated the ejecta deposits from various impact craters and basins. The yellow arrows indicate the ejecta thickness from different craters whose ejecta thickness is <1 m, red arrows indicate the ejecta thickness from 1 to 10 m, green arrow indicate >10 m. The blue arrows are the ejecta deposits from near and far impact basins. The SPA basin ejecta deposit at this site is ~1400 m. The white arrow indicated the ejecta deposits from secondary craters near the CH-3 site. The while dashed line is the SPA basin rim.

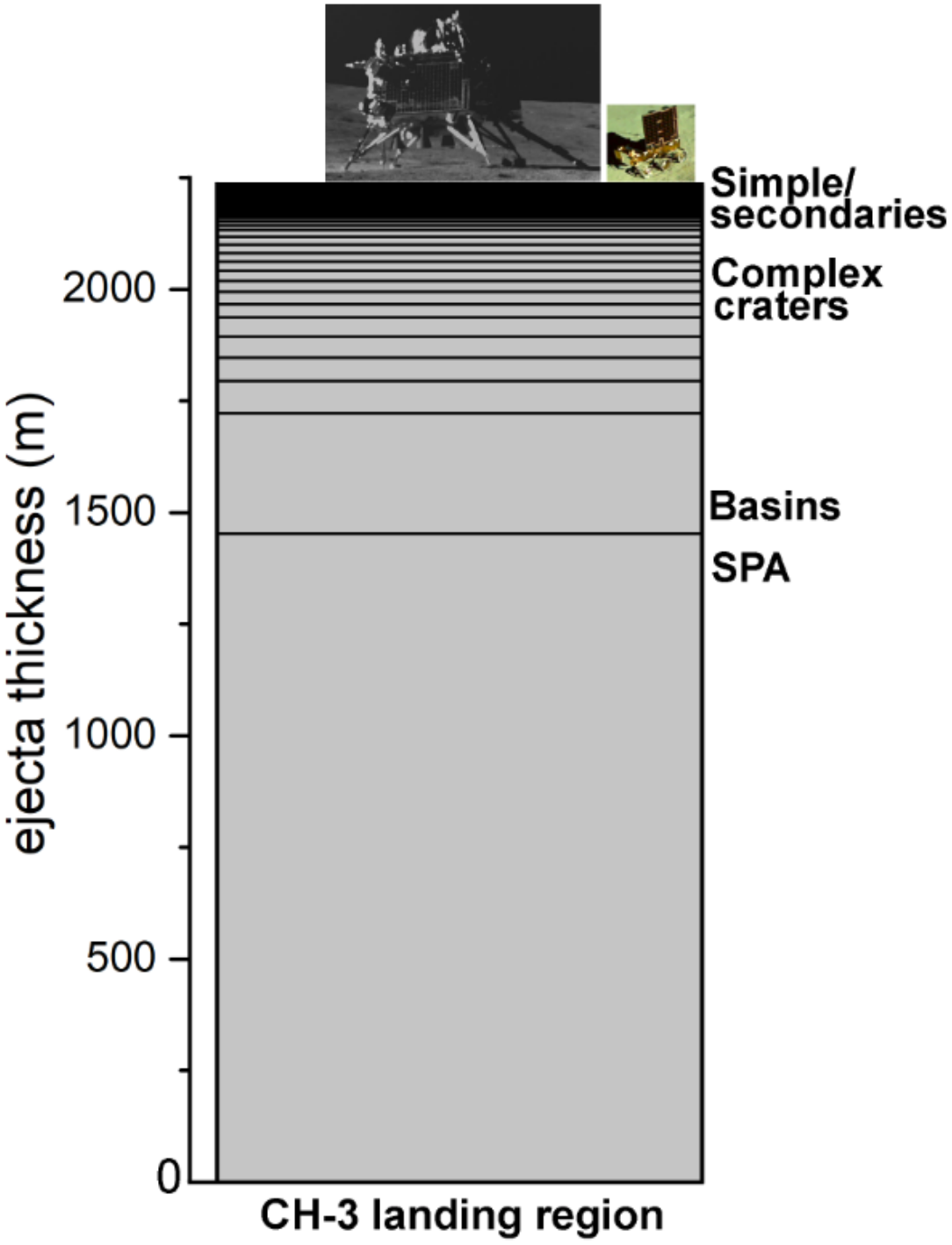

Fig. 6 The stratigraphy of ejecta deposits at the Chandrayaan-3 landing site by various impact basins and craters. The SPA basin ejecta dominates the landing site, whereas the complex craters and secondary churned the SPA ejecta and likely redistributed within the landing site. For the distribution of ejecta thickness for each impact refer to the Supplementary table 1.

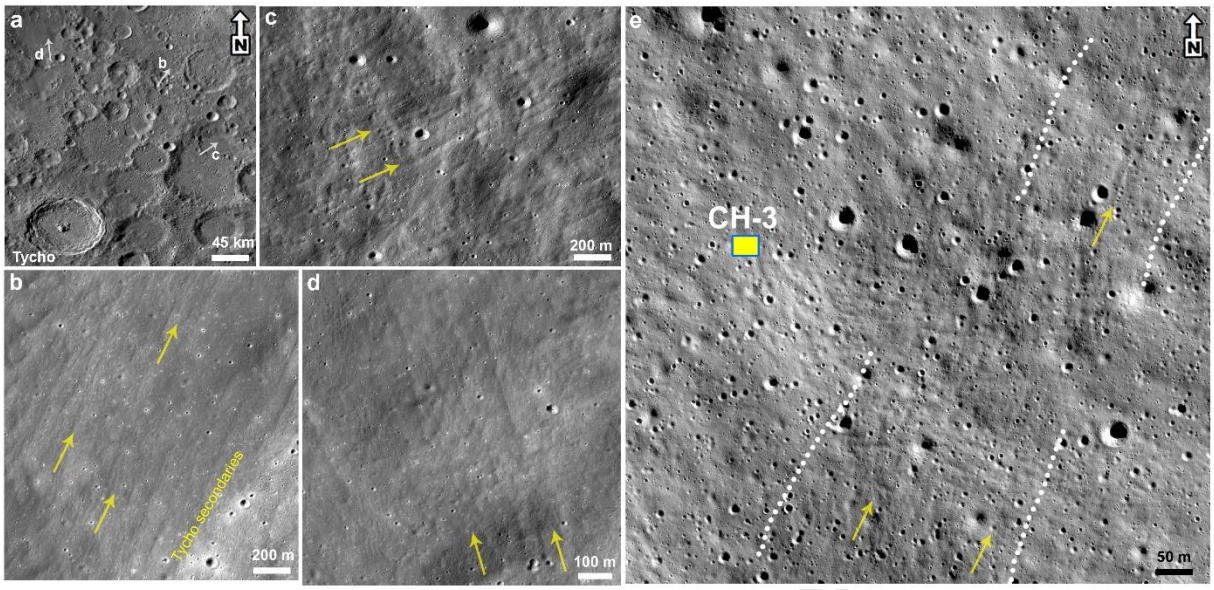

Fig. 7 Impact crater ejecta ray with linear groove-like structure a) Tycho crater and the distal ejecta, b) LRO-WAC image shows the distinguishable distal ejecta with linear, parallel grooves located at ~212 km from the Tycho rim. Note the Tycho secondaries are also aligned parallel to distal ejecta (-35.769° -6.159°), c) another location with distal ejecta linear, parallel grooves located at ~170 km from the rim (-39.340° -3.902°), d) another location to the North of Tycho crater with distal ejecta located at ~230 km from the rim (-34.150° -12.203°), c) Ch-2 OHRC image of the CH-3 landing site, similar linear, parallel grooves extending from SW to NE side and spread to several 100s of meters. These features indicate ejecta from distant impacts was emplaced over the landing site.

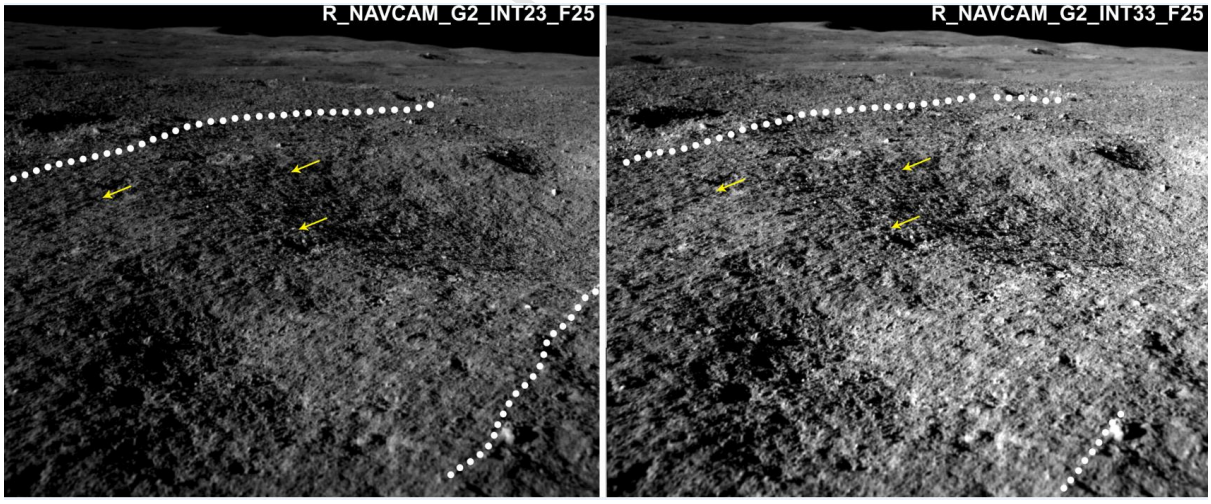

Fig. 8 The Pragyan rover Navcam images taken from the south of Vikram lander taken at two different integration time enhances the linear ray-like feature present over the landing site. These linear ray-like features are observed within a shallow crater and outside terrain too. Such features are also observed in two other locations that refer to Supplementary figures.

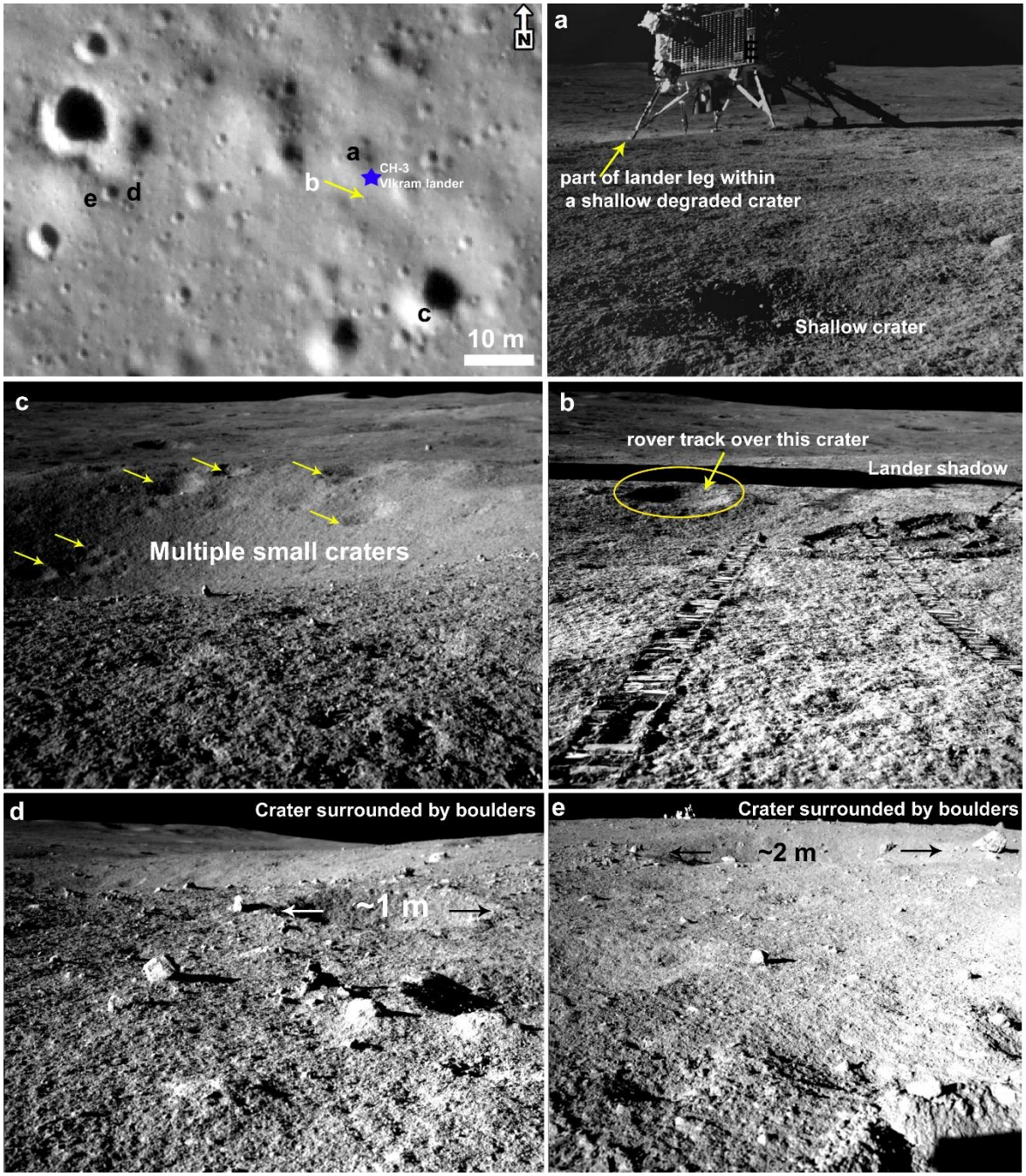

Fig. 9 Top left image shows the CH-2 OHRC image of the landing site. a) The Vikram lander one of the legs partially within a shallow crater, and lacks any boulder over that region, b) Vikram lander shadow and a shallow crater adjacent to it. Through this small crater the rover made its traverse and the track is also visible from the crater walls. This indicates a shallow crater over this region. c) A part of ~10 m crater located south of Vikram lander, multiple superposed craters are observed in the walls. This crater lacks boulders and rims are smooth suggesting their old nature, d) crater surrounded by boulders and e) several craters surrounded by boulders and Vikram lander and large boulders seen in the horizon. Such boulders are present over the west side of the lander.

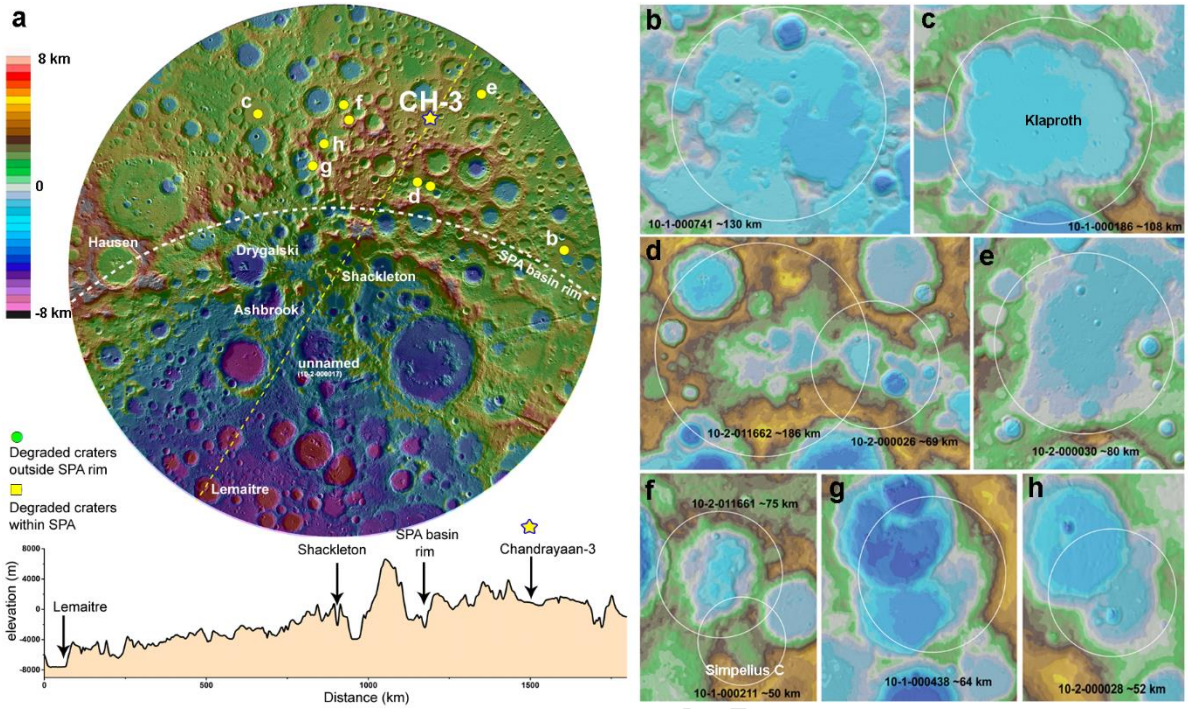

Fig. 10 a) LRO-WAC stereographic image overlaid on WAC-DEM for the south polar region. Several craters are degraded over this region, the SPA basin rim demarcates the degraded crater within the SPA basin and outside the basin. b-h) degraded impact crater located outside the SPA basin rim, whose rims are heavily degraded and they are relatively shallow in depth. Such craters are widespread in the south pole region. All the craters are cataloged by Robbins (2019).

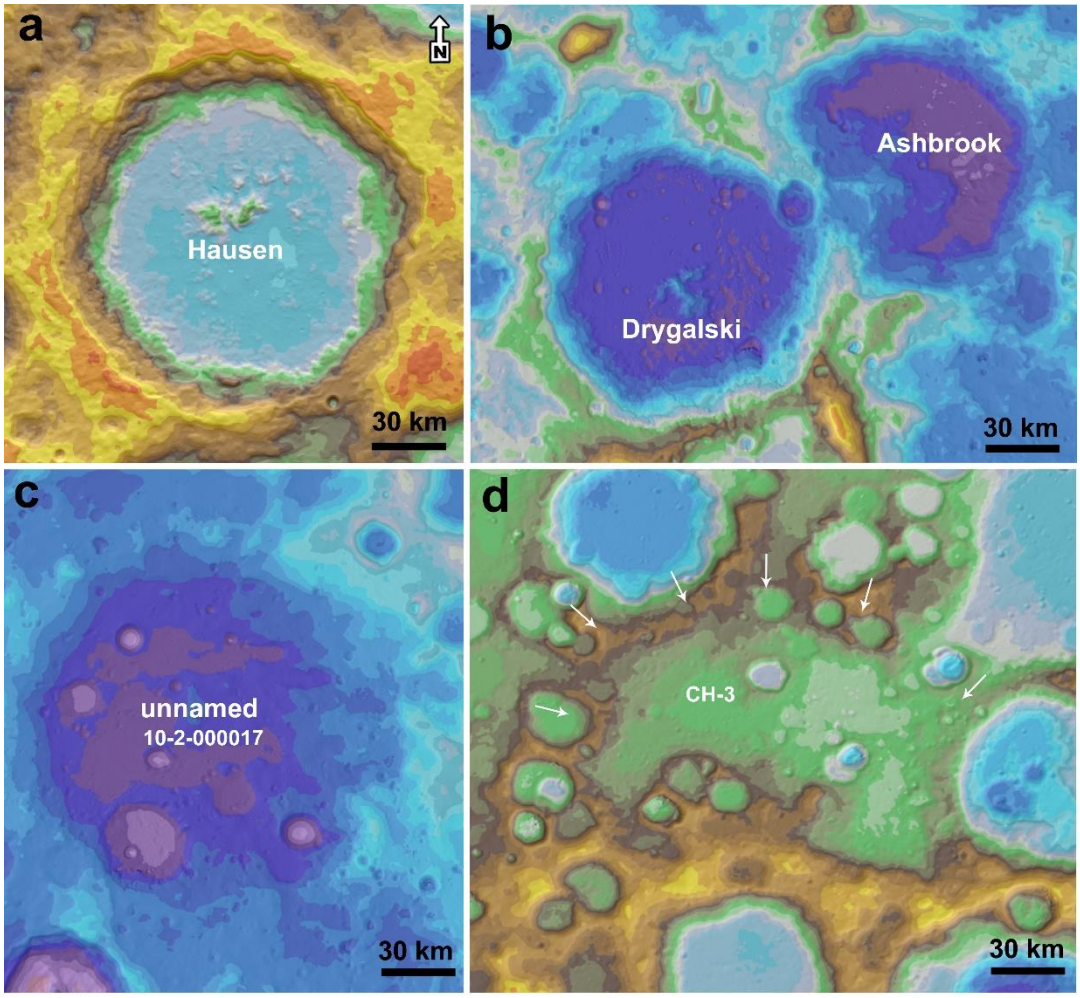

Fig. 11 A set of examples impact crater with diameter >150 km a) Hausen crater with preserved rim, peaks and ejecta, b) Drygalski crater superposed the Ashbrook crater and degraded the later one. Such degradation along with the rim erasure also decreases the crater depth by depositing ejecta over it. c) an unnamed crater located to the west of Schrodinger basin (Location of these craters are shown in Fig. 10a). This unnamed crater is prior to Schrodinger and degraded by the later impact and highly degraded. d) a semi-circular structure observed around the Ch-3 landing site. This could be probably a buried impact crater. The SPA basin ejecta and the other complex crater lead to severe degradation. For the locations of these crater refer to Fig.10 and for topographic profile refer to Fig. S18.

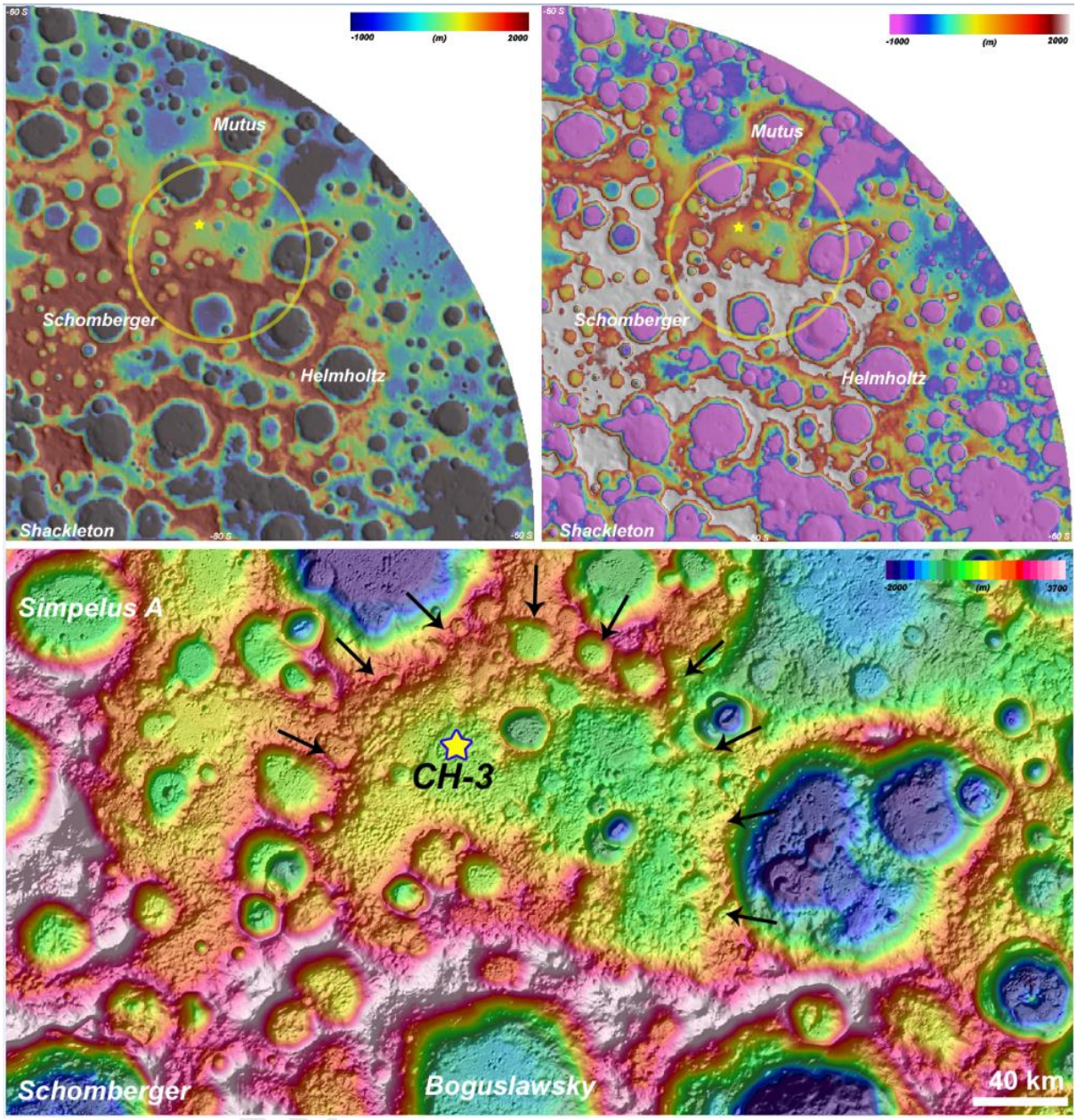

Fig. 12 a, b) The areal distribution of the South polar region with the Chandrayaan-3 landing zone from SLDEM with masked elevation zones to highlight the buried crater over the Chandrayaan-3 landing site, c) The SLDEM draped over the hill shade image to highlight the buried semi-circular structure over the Chandrayaan-3 landing site region.

References

Barker, M. K., E. Mazarico, G. A. Neumann, M. T. Zuber, J. Haruyama, and D. E. Smith. 2016. "A New Lunar Digital Elevation Model from the Lunar Orbiter Laser Altimeter and SELENE Terrain Camera." Icarus 273:346–55. doi: 10.1016/j.icarus.2015.07.039.

Basilevskii, A.T., 1976, April. On the evolution rate of small lunar craters. In In: Lunar Science Conference, 7th, Houston, Tex., March 15-19, 1976, Proceedings. Volume 1.(A77-34651 15-91) New York, Pergamon Press, Inc., 1976, p. 1005-1020. (Vol. 7, pp. 1005-1020).

Bierhaus, Edward B., Luke Dones, José Luis Alvarellos, and Kevin Zahnle. 2012. "The Role of Ejecta in the Small Crater Populations on the Mid-Sized Saturnian Satellites." Icarus 218(1):602–21. doi: 10.1016/j.icarus.2011.12.011.

Carrier III, W.D., 1974. Apollo drill core depth relationships. The moon, 10(2), pp.183-194.

Chowdhury, Arup Roy, Manish Saxena, Ankush Kumar, S. R. Joshi, Aditya Dagar Amitabh, Manish Mittal, Shweta Kirkire, Jalshri Desai, Dhrupesh Shah, and J. C. Karelia. 2019. "Orbiter High Resolution Camera Onboard Chandrayaan-2 Orbiter." Current Science 117(7):560.

Clegg, R.N., Jolliff, B.L., Robinson, M.S., Hapke, B.W. and Plescia, J.B., 2014. Effects of rocket exhaust on lunar soil reflectance properties. Icarus, 227, pp.176-194.

Dundas, Colin M., and Alfred S. McEwen. 2007. "Rays and Secondary Craters of Tycho." Icarus 186(1):31–40. doi: 10.1016/j.icarus.2006.08.011.

Elliott, J.R., Huang, Y.H., Minton, D.A. and Freed, A.M., 2018. The length of lunar crater rays explained using secondary crater scaling. Icarus, 312, pp.231-246.

Eliason, E., Isbell, C., Lee, E., Becker, T., Gaddis, L., McEwen, A. and Robinson, M., 1999. The Clementine UVVIS global lunar mosaic. Lunar and Planetary Institute, Houston.

Eggleton, R. E., and G. G. Schaber. 1972. "Cayley Formation Interpreted as Basin Ejecta, Part B." NASA. Lyndon B. Johnson Space Center Apollo 16 Prelim. Sci. Rept.

Fassett, Caleb I., James W. Head, David E. Smith, Maria T. Zuber, and Gregory A. Neumann. 2011. "Thickness of Proximal Ejecta from the Orientale Basin from Lunar Orbiter Laser Altimeter (LOLA) Data: Implications for Multi-Ring Basin Formation." Geophysical Research Letters 38(17). doi: 10.1029/2011GL048502.

Fassett, C.I., Head, J.W., Kadish, S.J., Mazarico, E., Neumann, G.A., Smith, D.E. and Zuber, M.T., 2012. Lunar impact basins: Stratigraphy, sequence and ages from superposed impact crater populations measured from Lunar Orbiter Laser Altimeter (LOLA) data. Journal of Geophysical Research: Planets, 117(E12).

Freeman V. L. (1981) F. Regolith of the Apollo 16 site. Geology of the Apollo 16 Area, Central Lunar Highlands. Geological Survey Professional Paper 1048 (eds. George E. Ulrich, Carroll Ann Hodges and William R. Muehlberger). US Government Printing Office, Washington

Fortezzo, c. M., p. D. Spudis, and s. L. Harrel. 2020. “release of the digital unified global geologic map of the moon at 1:5,000,000-.”

Fruland, R.M., Morris, R.V., McKay, D.S. and Clanton, U.S., 1977. Apollo 17 ropy glasses. In In: Lunar Science Conference, 8th, Houston, Tex., March 14-18, 1977, Proceedings. Volume 3.(A78-41551 18-91) New York, Pergamon Press, Inc., 1977, p. 3095-3111. (Vol. 8, pp. 3095-3111).

Kawashima, O., Morota, T., Ohtake, M. and Kasahara, S., 2022. Size–frequency measurements of meter-sized craters and boulders in the lunar polar regions for landing-site selections of future lunar polar missions. Icarus, 378, p.114938.

Krasilnikov, A.S., Krasilnikov, S.S., Ivanov, M.A. and Head, J.W., 2023. Estimation of Ejecta Thickness from Impact Craters in the South Polar Region of the Moon. Solar System Research, 57(2), pp.122-132.

Kring, D.A. and Durda, D., 2012. A global lunar landing site study to provide the scientific context for exploration of the Moon.

Gault, Donald E. 1970. “Saturation and Equilibrium Conditions for Impact Cratering on the Lunar Surface: Criteria and Implications.” Radio Science 5(2):273–91. doi: 10.1029/RS005i002p00273.

Guo, D., Liu, J., Head III, J.W. and Kreslavsky, M.A., 2018. Lunar Orientale impact basin secondary craters: Spatial distribution, size-frequency distribution, and estimation of fragment size. Journal of Geophysical Research: Planets, 123(6), pp.1344-1367.

Hawke, B.R., Blewett, D.T., Lucey, P.G., Smith, G.A., Bell III, J.F., Campbell, B.A. and Robinson, M.S., 2004. The origin of lunar crater rays. Icarus, 170(1), pp.1-16.

Head, James W. 1974. “Orientale Multi-Ringed Basin Interior and Implications for the Petrogenesis of Lunar Highland Samples.” The Moon 11(3–4):327–56. doi: 10.1007/BF00589168.

Head, J.W., 1975. Processes of lunar crater degradation: Changes in style with geologic time. The Moon, 12(3), pp.299-329.Head III, J.W., Fassett, C.I., Kadish, S.J., Smith, D.E., Zuber, M.T., Neumann, G.A. and Mazarico, E., 2010. Global distribution of large lunar craters: Implications for resurfacing and impactor populations. science, 329(5998), pp.1504-1507.

Hiesinger, H.V., Van Der Bogert, C.H., Pasckert, J.H., Funcke, L., Giacomini, L., Ostrach, L.R. and Robinson, M.S., 2012. How old are young lunar craters?. Journal of Geophysical Research: Planets, 117(E12).

Housen, K. R., R. M. Schmidt, and K. A. Holsapple. 1983. “Crater Ejecta Scaling Laws: Fundamental Forms Based on Dimensional Analysis.” *Journal of Geophysical Research: Solid Earth* 88(B3):2485–99. doi: 10.1029/JB088iB03p02485.

Howard, K.A., Wilhelms, D.E. and Scott, D.H., 1974. Lunar basin formation and highland stratigraphy. Reviews of Geophysics, 12(3), pp.309-327.

Huang, J., Xiao, Z., Flahaut, J., Martinot, M., Head, J., Xiao, X., Xie, M. and Xiao, L., 2018. Geological characteristics of Von Kármán crater, northwestern south pole-Aitken Basin: Chang'E-4 landing site region. Journal of Geophysical Research: Planets, 123(7), pp.1684-1700.

Hurwitz, D.M. and Kring, D.A., 2014. Differentiation of the South Pole–Aitken basin impact melt sheet: Implications for lunar exploration. Journal of Geophysical Research: Planets, 119(6), pp.1110-1133.

Ivanov, Mikhail, Albert Abdrakhimov, Alexander Basilevsky, N. Demidov, Evgeniya Guseva, James Head, H. Hiesinger, A. Kohanov, and Sergey Krasilnikov. 2017. Sources of Materials at the Three High-Priority Landing Sites of the Luna-Glob Mission.

Jolliff, B. L., and L. A. Haskin. 1995. "Cogenetic Rock Fragments from a Lunar Soil: Evidence of a Ferroan Noritic-Anorthosite Pluton on the Moon." Geochimica et Cosmochimica Acta 59(11):2345–74. doi: 10.1016/0016-7037(95)00110-L.

Kirchoff, M.R., Chapman, C.R., Marchi, S., Curtis, K.M., Enke, B. and Bottke, W.F., 2013. Ages of large lunar impact craters and implications for bombardment during the Moon's middle age. Icarus, 225(1), pp.325-341.

Krasilnikov, A.S., Krasilnikov, S.S., Ivanov, M.A. and Head, J.W., 2023. Estimation of Ejecta Thickness from Impact Craters in the South Polar Region of the Moon. Solar System Research, 57(2), pp.122-132.

Laha, J., Dinesh, B., Selvaraj, P. and Krishnamoorthy, S., 2018. Realization of Space Grade Miniature Digital Camera for Lunar Navigation. International Journal of Pure and Applied Mathematics, 118(6), pp.1105-1116.

Laxmiprasad, A.S., Raja, V.S., Menon, S., Goswami, A., Rao, M.V.H. and Lohar, K.A., 2013. An in situ laser induced breakdown spectroscope (LIBS) for Chandrayaan-2 rover: Ablation kinetics and emissivity estimations. Advances in Space Research, 52(2), pp.332-341.

Langevin, Y. and Arnold, J.R., 1977. The evolution of the lunar regolith. Annual Review of Earth and Planetary Sciences, 5(1), pp.449-489.

Le Mouélic, Stéphane, P. G. Lucey, Yves Langevin, and B. Ray Hawke. 2002. "Calculating Iron Contents of Lunar Highland Materials Surrounding Tycho Crater from Integrated Clementine UV-Visible and near-Infrared Data." Journal of Geophysical Research: Planets 107(E10):4-1-4–9. doi: 10.1029/2000JE001484.

Mahanti, P., M. S. Robinson, T. J. Thompson, and M. R. Henriksen. 2018. "Small Lunar Craters at the Apollo 16 and 17 Landing Sites - Morphology and Degradation." Icarus 299:475–501. doi: 10.1016/j.icarus.2017.08.018.

McGetchin, T. R., M. Settle, and J. W. Head. 1973. "Radial Thickness Variation in Impact Crater Ejecta: Implications for Lunar Basin Deposits." Earth and Planetary Science Letters 20(2):226–36. doi: 10.1016/0012-821X(73)90162-3.

McKay, D.S., Heiken, G., Basu, A., Blanford, G., Simon, S., Reedy, R., French, B.M. and Papike, J., 1991. The lunar regolith. Lunar sourcebook, 567, pp.285-356.

Melosh, H. J. 1989. “Impact Cratering : A Geologic Process.” New York : Oxford University Press ; Oxford : Clarendon Press.

Meyer, H. M., B. W. Denevi, M. S. Robinson, and A. K. Boyd. 2020. “The Global Distribution of Lunar Light Plains From the Lunar Reconnaissance Orbiter Camera.” Journal of Geophysical Research: Planets 125(1):e2019JE006073. doi: 10.1029/2019JE006073.

Melosh, H. J., Kendall, J., Horgan, B., Johnson, B., Bowling, T., Lucey, P., & Taylor, G. (2017). South Pole–Aitken basin ejecta reveal the Moon’s upper mantle. Geology, 45(12), 1063–1066.

Mithun, N.P.S., Vadawale, S.V., Shanmugam, M., Patel, A.R., Singh, N., Kumar, S., Tiwari, N.K., Goyal, S.K., Sarbadhikari, A.B., Arora, G. and Srivastava, Y., 2020. Ground calibration of Alpha Particle X-ray Spectrometer (APXS) on-board Chandrayaan-2 Pragyaan rover: An empirical approach. Planetary and Space Science, 187, p.104923.

Moriarty, D. P., & Pieters, C. M. (2018). The character of south pole - Aitken Basin: Patterns of surface and sub-surface composition. Journal of Geophysical Research: Planets, 123, 729–747

Moriarty III, D.P., Dygert, N., Valencia, S.N., Watkins, R.N. and Petro, N.E., 2021. The search for lunar mantle rocks exposed on the surface of the Moon. Nature Communications, 12(1), p.4659.

Moriarty Iii, D.P., Watkins, R.N., Valencia, S.N., Kendall, J.D., Evans, A.J., Dygert, N. and Petro, N.E., 2021. Evidence for a stratified upper mantle preserved within the South Pole-Aitken Basin. Journal of Geophysical Research: Planets, 126(1), p.e2020JE006589.

Muehlberger, W. R., R. M. Batson, E. L. Boudette, C. M. Duke, R. E. Eggleton, D. P. Elston, A. W. England, V. L. Freeman, M. H. Hait, and T. A. Hall. 1972. “Preliminary Geologic Investigation of the Apollo 16 Landing Site.” Pp. 6–1 in Apollo 16 Preliminary Science Report. NASA SP-315 Washington, DC.

Neukum, G., König, B. and Arkani-Hamed, J., 1975. A study of lunar impact crater size-distributions. The moon, 12(2), pp.201-229.

Oberbeck, Verne R. 1973. Emplacement of the Cayley Formation. Vol. 62302. National Aeronautics and Space Administration.

Oberbeck, V.R., 1975. The role of ballistic erosion and sedimentation in lunar stratigraphy. Reviews of Geophysics, 13(2), pp.337-362.

Osinski, G.R., Tornabene, L.L. and Grieve, R.A., 2011. Impact ejecta emplacement on terrestrial planets. Earth and Planetary Science Letters, 310(3-4), pp.167-181.

Osinski, G.R., Grieve, R.A., Ferrière, L., Losiak, A., Pickersgill, A.E., Cavosie, A.J., Hibbard, S.M., Hill, P.J., Bermudez, J.J., Marion, C.L. and Newman, J.D., 2022. Impact Earth: A review of the terrestrial impact record. Earth-Science Reviews, 232, p.104112.

Petro, N. E., and C. M. Pieters. 2006. “Modeling the Provenance of the Apollo 16 Regolith.” Journal of Geophysical Research: Planets 111(E9). doi: 10.1029/2005JE002559.

Pike, Richard J. 1974. “Ejecta from Large Craters on the Moon: Comments on the Geometric Model of McGetchin et Al.” Earth and Planetary Science Letters 23(3):265–71. doi: 10.1016/0012-821X(74)90114-9.

Povilaitis, R. Z., M. S. Robinson, C. H. van der Bogert, H. Hiesinger, H. M. Meyer, and L. R. Ostrach. 2018. “Crater Density Differences: Exploring Regional Resurfacing, Secondary Crater Populations, and Crater Saturation Equilibrium on the Moon.” Planetary and Space Science 162:41–51. doi: 10.1016/j.pss.2017.05.006.

Riedel, Christian, David A. Minton, Gregory Michael, Csilla Orgel, Carolyn H. van der Bogert, and Harald Hiesinger. 2020. “Degradation of Small Simple and Large Complex Lunar Craters: Not a Simple Scale Dependence.” Journal of Geophysical Research: Planets 125(4):e2019JE006273. doi: 10.1029/2019JE006273.

Robbins, Stuart J. 2019. “A New Global Database of Lunar Impact Craters >1–2 Km: 1. Crater Locations and Sizes, Comparisons With Published Databases, and Global Analysis.” Journal of Geophysical Research: Planets 124(4):871–92. doi: 10.1029/2018JE005592.

Roberts, L., 1963. Visibility and dust erosion during the lunar landing. A compilation of recent research related to the Apollo Mission, pp.155-170.

Schultz, Peter H., and Jill Singer. n.d. “A Comparison of Secondary Craters on the Moon, Mercury, and Mars.”

Scott, David H., John F. McCauley, and Mareta N. West. n.d. “GEOLOGIC MAP OF THE WEST SIDE OF THE MOON.”

Sharpton, Virgil L. 2014. “Outcrops on Lunar Crater Rims: Implications for Rim Construction Mechanisms, Ejecta Volumes and Excavation Depths.” Journal of Geophysical Research: Planets 119(1):154–68. doi: 10.1002/2013JE004523.

Sinha, R.K., Sivaprahasam, V., Bhatt, M., Kumari, N., Srivastava, N., Varatharajan, I., Ray, D., Wöhler, C. and Bhardwaj, A., 2020. Geological characterization of Chandrayaan-2 landing site in the southern high latitudes of the Moon. Icarus, 337, p.113449.

Sinha, R.K., Rani, A., Ruj, T. and Bhardwaj, A., 2023. Geologic investigation of lobate scarps in the vicinity of Chandrayaan-3 landing site in the southern high latitudes of the moon. Icarus, 402, p.115636.

Speyerer, Emerson J., Reinhold Z. Povilaitis, Mark S. Robinson, Peter C. Thomas, and Robert V. Wagner. 2016. “Quantifying Crater Production and Regolith Overturn on the Moon with Temporal Imaging.” Nature 538(7624):215–18. doi: 10.1038/nature19829.

Subhalakshmi, K., Basavaraj, B., Selvaraj, P. and Laha, J., 2010, December. Design of Miniature Space Grade Navigation Camera for Lunar Mission. In 2010 International Symposium on Electronic System Design (pp. 169-174). IEEE.

Trask, Newell J., and John F. McCauley. 1972. “Differentiation and Volcanism in the Lunar Highlands: Photogeologic Evidence and Apollo 16 Implications.” Earth and Planetary Science Letters 14(2):201–6.

Uemoto, K., Ohtake, M., Haruyama, J., Matsunaga, T., Yamamoto, S., Nakamura, R., Yokota, Y., Ishihara, Y. and Iwata, T., 2017. Evidence of impact melt sheet differentiation of the lunar South Pole-Aitken basin. Journal of Geophysical Research: Planets, 122(8), pp.1672-1686.

Vadawale, et al., 2024. Chandrayaan-3 APXS elemental abundance measurements at lunar high latitude. Nature, 633, pp 327–331.

Watters, W.A., Zuber, M.T. and Hager, B.H., 2009. Thermal perturbations caused by large impacts and consequences for mantle convection. Journal of Geophysical Research: Planets, 114(E2).

Watters, T.R., Schmerr, N.C., Weber, R.C., Johnson, C.L., Speyerer, E.J., Robinson, M.S. and Banks, M.E., 2024. Tectonics and Seismicity of the Lunar South Polar Region. The Planetary Science Journal, 5(1), p.22.

Wang, Y., Wu, B., Xue, H., Li, X. and Ma, J., 2021. An improved global catalog of lunar impact craters (≥ 1 km) with 3D morphometric information and updates on global crater analysis. Journal of Geophysical Research: Planets, 126(9), p.e2020JE006728.

Watkins, R.N., Jolliff, B.L., Mistick, K., Fogerty, C., Lawrence, S.J., Singer, K.N. and Ghent, R.R., 2019. Boulder distributions around young, small lunar impact craters and implications for regolith production rates and landing site safety. Journal of Geophysical Research: Planets, 124(11), pp.2754-2771.

Wilhelms, D. E. 1965. “Fra Mauro and Cayley Formations in the Mare Vaporum and Julius Caesar Quadrangles.” Astrogeologic Studies Annual Progress Report. July 1(1964):13–28.

Wilhelms, Don E. 1970. Summary of Lunar Stratigraphy-Telescopic Observations.

Wilhelms et al., 1987 The geological history of the Moon, U.S. Geol. Survey, Prof. Paper 1347.

Woronow, A. 1978. “A General Cratering-History Model and Its Implications for the Lunar Highlands.” Icarus 34(1):76–88. doi: 10.1016/0019-1035(78)90127-6.

Wu, B., Wang, Y., Werner, S.C., Prieur, N.C. and Xiao, Z., 2022. A global analysis of crater depth/diameter ratios on the Moon. Geophysical Research Letters, 49(20), p.e2022GL100886.

Xiao, Zhiyong, Chunyu Ding, Minggang Xie, Yuzhen Cai, Jun Cui, Ke Zhang, and Juntao Wang. 2021. “Ejecta From the Orientale Basin at the Chang’E-4 Landing Site.” Geophysical Research Letters 48(3):e2020GL090935. doi: 10.1029/2020GL090935.

Xie, Minggang, Tiantian Liu, and Aoao Xu. 2020. “Ballistic Sedimentation of Impact Crater Ejecta: Implications for the Provenance of Lunar Samples and the Resurfacing Effect of Ejecta on the Lunar Surface.” Journal of Geophysical Research: Planets 125(5):e2019JE006113. doi: 10.1029/2019JE006113.

Xie, Minggang, and Meng-Hua Zhu. 2016. “Estimates of Primary Ejecta and Local Material for the Orientale Basin: Implications for the Formation and Ballistic Sedimentation of Multi-Ring Basins.” Earth and Planetary Science Letters 440:71–80.

Xu, L. and Xie, M., 2020. Ejecta thickness distribution of the Schrödinger Basin on the Moon. Journal of Geophysical Research: Planets, 125(12), p.e2020JE006506.

Declaration of interests

☒ The authors declare that they have no known competing financial interests or personal relationships that could have appeared to influence the work reported in this paper.

☐ The author is an Editorial Board Member/Editor-in-Chief/Associate Editor/Guest Editor for *[Journal name]* and was not involved in the editorial review or the decision to publish this article.

☐ The authors declare the following financial interests/personal relationships which may be considered as potential competing interests:

Dr. Vijayan S

Physical Research Laboratory

Highlights

- Chandrayaan-3 Pragyan rover images analysed for the first insitu crater distribution at Lunar high latitude south polar region
- Chandrayaan-3 Vikram lander landed over ~2300 m of ejecta deposited from the South Pole Aitken basin and other basins/craters
- Chandrayaan-3 mission landed within a buried impact crater, which is likely older than SPA basin